Check for updates

ADVANCED ELECTRONIC MATERIALS
www.advelectronicmat.de

Geometric Study of Polymer Embedded Micro Thermoelectric Cooler with Optimized Contact Resistance

Aditya S. Dutt, Kangfa Deng, Guodong Li, Nithin B Pulumati, David Alberto Lara Ramos, Vida Barati, Javier Garcia, Nicolas Perez, Kornelius Nielsch, Gabi Schierning, and Heiko Reith**

Micro-thermoelectric devices (μTEDs) are used for bio-medical applications, powering internet-of-things devices, and thermal management. For such applications, μTEDs need to have a robust packaging so that the devices can be brought in direct thermal contact with the target heat sink and source. The packaging technology developed for macroscopic modules needs improvement as it cannot be applied to μTEDs due to a large thermal resistance between the capping material and the device which deteriorates its performance. In this work, μTEDs with high net cooling temperature are fabricated by optimizing the contact resistance and device design combined with a novel packaging technique that is fully compatible with on-chip integration. The simulations and experiments demonstrate that the additional thermal loss caused by the packaging leads to an only marginal decrease in the net cooling temperature. The devices achieve a high net cooling temperature of 10.8 K without packaging and 9.6 K with packaging at room temperature. The packaging only slightly increases the thermal response time of the devices, which also shows an extremely high reliability of over 85 million cooling cycles. This simple packaging technique together with robust device performance is a step toward wide-spread application of μTEDs.

1. Introduction

Micro-thermoelectric devices (μTEDs) directly convert heat fluxes into electrical energy, or vice versa. They work without any moving parts and are thus maintenance free, and also environment-friendly.[1–4] They are used for the thermal management of parts of electric circuits[5] or optoelectronic devices,[6] cooling of power electronics,[7] powering devices for the internet-of-things,[8] and body-powered wearable electronics.[9–11] With increased reliability and accurate temperature control, they could also be effective replacements for macroscopic thermoelectric devices (TEDs) in medical applications,[12–14] for example DNA replication[15] or heating and cooling experiments for treating low-grade tissue injuries.[16]

Early μTEDs were fabricated by J.-P. Fleurial and co-workers.[17] During the past two decades, as the approaches to fabrication have evolved continuously, so has the performance of μTEDs.[1,2,18–20] In 2003, Snyder et al. fabricated a cross plane μTED using electrochemical deposition, which showed a maximum cooling of 2 K at 110 mA.[2] μTEDs based on superlattice materials were later fabricated but were not characterized as coolers.[21] In 2007, Huang et al. fabricated a device using MEMS technology in combination with electroplating and reported a maximum cooling of

A. S. Dutt, K. Deng, G. Li, N. B. Pulumati, D. A. L. Ramos, V. Barati, N. Perez, K. Nielsch, H. Reith
Institute for Metallic Materials
Leibniz Institute for Solid State and Materials Research Dresden
Helmholtzstrasse 20, 01069 Dresden, Germany
E-mail: h.reith@ifw-dresden.de

A. S. Dutt, N. B. Pulumati, D. A. L. Ramos, V. Barati, K. Nielsch
Institute of Materials Science
Dresden University of Technology
01062 Dresden, Germany

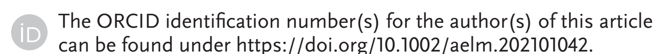
The ORCID identification number(s) for the author(s) of this article can be found under https://doi.org/10.1002/aelm.202101042.

© 2022 The Authors. Advanced Electronic Materials published by Wiley-VCH GmbH. This is an open access article under the terms of the Creative Commons Attribution-NonCommercial-NoDerivs License, which permits use and distribution in any medium, provided the original work is properly cited, the use is non-commercial and no modifications or adaptations are made.

DOI: 10.1002/aelm.202101042

G. Li
Beijing National Laboratory for Condensed Matter Physics
Institute of Physics
Chinese Academy of Sciences
Beijing 100190, China
E-mail: gdli@iphy.ac.cn

D. A. L. Ramos
Consejo Nacional de Ciencia y Tecnologia Av. Insurgentes Sur 1582
Col. Crédito Constructor
Del. Benito Juárez, Ciudad de México 03940, México

J. Garcia
Department of Physics
University of Oviedo
Oviedo 33007, Spain

K. Nielsch
Institute of Applied Physics
TU Dresden
01062 Dresden, Germany

G. Schierning
Department of Physics
Experimental Physics
Bielefeld University
100131 Bielefeld, Germany

0.7 K using infrared imaging.[22] Later in 2008, the same group improved the net cooling temperature to 1.2 K.[23] In 2013, Roth et al. developed a flip chip bonding process and fabricated a device using two different substrates but was not characterized as coolers.[24] A startup company called Micropelt fabricated µTEDs using flip chip bonding in combination with sputtering, which proves to be an expensive technique.[25] Later in 2021, a thin film µTED with extreme heat flux handling was demonstrated.[26] In this work, we report on the fabrication of µTEDs based on electrochemical deposition, a cost-effective method that works at room temperature without vacuum to synthesize materials with desired composition and crystalline structure. The most important performance measure of a thermoelectric material is its thermoelectric figure of merit $zT = (S^2\ \sigma\ \kappa^{-1})\ T$, where S is the Seebeck coefficient; σ is the electrical conductivity; κ is the total thermal conductivity; and T is the absolute temperature.[27,28] The performance of thermoelectric materials has improved dramatically in recent years: for instance, zT was improved from around 1[29] in bismuth telluride and bismuth selenide systems to 2.6 in SnSe single crystals.[30] Although the performance of thermoelectric materials has improved greatly, that has not necessarily led to a substantial improvement in the performance of the devices themselves. This is because the performance also depends on the design and assembly of the TEDs.[31] The performance of TEDs themselves is characterized by the device figure of merit $ZT = (S_p - S_n)^2\ T\ (RK)^{-1}$, where S_p and S_n are the Seebeck coefficients of p-type and n-type legs; R is the electrical resistance of the device (including the contact resistance and the resistance of the metallization); and K is the thermal conductance of the device (including the thermal conductance of contact material and that of the metallization).[32] For optimized thermoelectric performance, aside from highest possible zT, it is also important to have excellent electrical contacts, thermal interfaces, mechanical properties, interconnects, and packaging technology.

The importance of packaging technology is often neglected in the fabrication of thermoelectric coolers (TECs) generally and micro-TECs (µTECs) in particular. This insulating fillers in the gaps between the thermoelectric legs mechanically support the devices. The filling material prevents oxidation, improving the chemical stability. Because the packaging technology of macroscopic modules entails a large thermal resistance between the capping material and the device, it cannot be applied to µTECs without deteriorating their performance substantially.

Previously, our group fabricated a µTEC by a combination of electrochemical deposition and photolithography. This work assessed transient response and cooling stability as well as cycling reliability.[1] Here we show that by effectively optimizing the geometry and the contact resistance, we were able to obtain a greatly improved net cooling temperature by 80% as compared with previous work. Further, the fabricated device showed a record high cycling stability of 100 million cycles. We were able to reduce the device's contact resistance such that we obtained a cooling power density close to theoretical maximum when the contact resistance would be zero. As of our knowledge, this is the highest reported net cooling temperature and cycling stability of a µTEC fabricated using electrochemical deposition. We then embedded the µTECs in a low-κ polymer filling material. We found that the polymers gave mechanical integrity and chemical stability to the devices with an only marginal decrease in the net cooling temperature. Polymer embedded micro devices pave the way for a widespread application of thermoelectrics in modern electronics and for potential applications in bio medical field, that is, to study temperature effects even on single biological cells.

2. Experimental Section

2.1. Fabrication Technology

The devices were fabricated by using multiple steps of photolithography and electrochemical deposition. All photolithographic steps were done using a laserwriter (μPG 101, Heidelberg Instruments GmbH, Germany, 375 nm irradiation wavelength). The device was fabricated on a Si substrate, which was coated by a Si_3N_4 layer with a thickness of 100 nm. 5 nm Cr and 100 nm Au were sputtered on the substrate as the adhesion layer and as seed layer, respectively, for the electrochemical deposition. For the first lithography, an adhesion promoter (TI Prime, MicroChemicals GmbH, Germany), photoresist (AZ5214E, MicroChemicals GmbH, Germany), and developer (AZ 726 MIF, MicroChemicals GmbH, Germany) were used to pattern alignment markers and to structure the metallization layer of Cr/Au on desired parts of the substrate for the subsequent etching (**Figure 1**a). The Au was etched using a KI/I_2 solution and Cr was etched with a commercial Cr etchant solution (TechniEtch Cr01, MicroChemicals GmbH, Germany). After etching, the photoresist was removed using n-methyl pyrrolidone (NMP) and the remaining photoresist residues were removed by O_2 plasma. For the next photolithography (Figure 1b), a 10 µm thick photoresist (AZ9260, MicroChemicals GmbH, Germany) and developer (AZ 400K [1:4 solution], MicroChemicals GmbH, Germany) were used. After patterning and developing, 3 µm thick Au was electrochemically deposited on the patterned structures.

After removing the photoresist residues, the next structuring was done with 24 µm thick photoresist. Here, AZ9260 was used twice to get the desired thickness. n-type $Bi_2(Te_{0.95}Se_{0.05})_3$ (in the following referred to as BiTeSe) was electrochemically deposited into the cavities and the composition was determined by EDX. The thickness of the deposited material was 10 µm. After the n-type deposition, the sample was electrochemically deposited with 1 µm of Au (Figure 1c). Subsequently, p-type Te was deposited, together with 1 µm of electrodeposited Au on top of the Te legs (Figure 1d). After the deposition of thermoelectric legs, multiple photolithographic steps were used for depositing the top Au bridge. 24 µm thick AZ9260 was spin-coated on the substrate. After spin-coating, the photoresist was leveled at the same height as that of the thermoelectric legs by exposure to a smaller dose using µPG 101 and by controlling the development time (Figure 1e). After leveling, 40 nm Au film was sputtered on the sample, acting as a seed layer for the subsequent electrochemical deposition process and preventing the removal of leveled photoresist during further steps (Figure 1f). A 10-µm-thick photoresist was spin-coated on top of the sputtered Au film. Photolithography was performed for structuring the top bridge (Figure 1g). 6-µm-thick Au was electrochemically deposited into the cavities (see subchapter 4.2), followed by lift-off. After lift-off, a photolithographic process was done to structure the bottom contact on the substrate (Figure 1h).

© 2022 The Authors. Advanced Electronic Materials published by Wiley-VCH GmbH

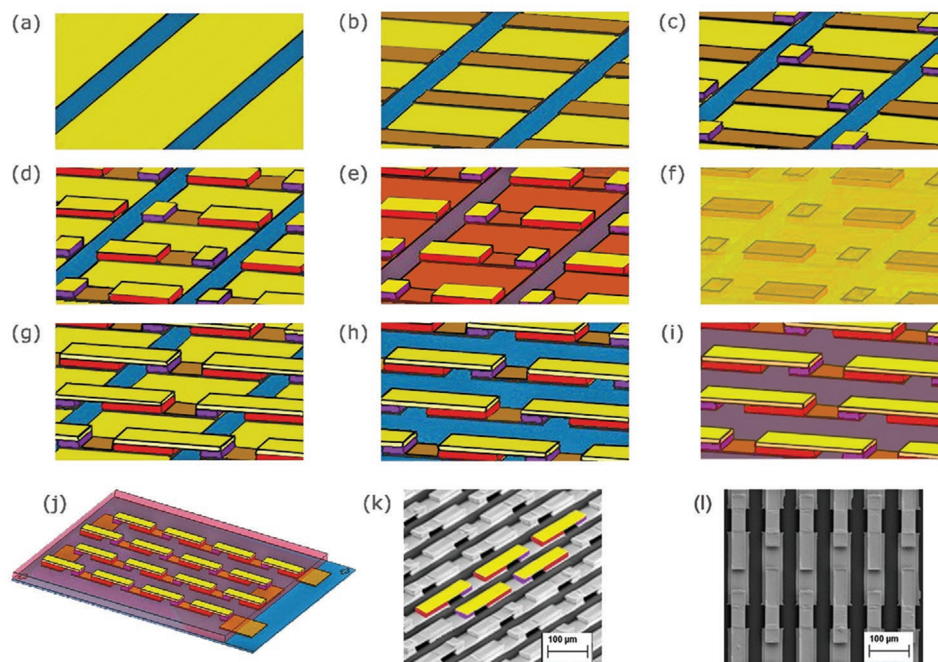

Figure 1. Schematic fabrication process of free-standing and embedded µTECs. a) Structuring the Au seed layer on a Si/Si_3N_4 substrate; b) Electrochemical deposition of 3 µm thick bottom Au electrode; c) Electrochemical deposition of 10 µm thick *n*-type BiTeSe and subsequent plating 1 µm thick Au top electrode on BiTeSe; d) Electrochemical deposition of 10 µm thick p-type Te and subsequent plating 1 µm thick Au top electrode on Te; e) Levelling the thermoelectric legs with AZ9260; f) Sputtering thin layer of Au; g) electrochemical deposition of 6 µm thick top Au; h) Free-standing µTEC; i) Polymer embedded µTEC; j) Graphical representation of polymer embedded µTEC; k) SEM image of µTEC (side view); l) SEM image of µTEC (top view).

To embed the as-fabricated free-standing device, AZ9260 was spin-coated twice. After spin-coating, the top Au portion was exposed and developed. Then leveling was done by exposure with a partial dose and by controlling the development time, thus achieving the polymer height in the desired range of the height of the device (Figure 1j). Finally, the whole device was embedded in a polymer matrix, that is, the polymer matrix forms a uniform top surface with the same height as the thermoelectric legs.

2.2. Electrochemical Deposition of Au, $Bi_2(Te_{0.95}Se_{0.05})_3$ and Te

Prior to all electrochemical depositions, the device was cleaned in O_2 plasma using a reactive ion etching (RIE) device (SI220 from Sentech Instruments GmbH, Germany) with an O_2 gas flow of 25 sccm at a power of 50 W for 2 min.

Thick Au films were used as bottom and top contacts for the device. Electrochemical deposition was used to get thicker Au films. The commercial electrolyte NB Semiplate Au 100 (NB Technologies GmbH, Germany) was used for the electrochemical deposition of thick Au films. The electrochemical deposition of Au was carried out in galvanostatic mode in a two-electrode configuration with a Pt counter electrode at room temperature using a VSP modular five channels potentiostat(Bio-Logic SAS, France). The current density was fixed at 18.35 $\mu A cm^{-2}$.

BiTeSe and Te were used as n-type and p-type thermoelectric materials. Both these materials were electrochemically synthesized from HNO_3 (Merck, 69%) based electrolytes. The chemicals used were $Bi(NO_3)_3 \cdot 5H_20$ (Merck, 99.999%), TeO_2 (Merck, 99.5%), SeO_2 (Strem chemicals, 99.8%). The electrolyte for BiTeSe was prepared by dissolution of 10 mM TeO_2 in 1M HNO_3 followed by the addition of 10 mM $Bi(NO_3)_3 \cdot 5H_20$ and 1.1 mM SeO_2. For the preparation of p-type Te electrolyte, 10 mM of TeO_2 was dissolved in 1M HNO_3. Just before electrochemically depositing Te, sodium dodecyl sulfate (SDS) was added as surfactant to the electrolyte to make the deposited thick film smoother.

The n-type and p-type electrochemical depositions were performed under pulsed potentiostatic conditions in a three-electrode configuration with a Pt counter electrode and Ag/AgCl reference electrode at room temperature using a modular five channels potentiostat. For the pulsed electrochemical deposition of BiTeSe, the deposition potential of $E_{on} = -0.015$ V was applied for t_{on} = 10 ms, followed by a reverse potential E_{off} = 0.186 V for t_{off} = 50 ms. For the pulsed electrochemical deposition of Te, the deposition potential of $E_{on} = -0.075$ V was applied for t_{on} = 10 ms, followed by a reverse potential E_{off} = 0.180 V for t_{off} = 50 ms.

To improve the quality of the thermoelectric materials, the oxygen saturation of the electrolyte was modified by bubbling the electrolyte with N_2 gas (5N quality) for 20 min prior to deposition for µTEC_4.

2.3. Thermoreflectance Microscopy

The characterization of the devices was done with charge coupled device based thermoreflectance microscopy. Thermoreflectance microscopy was a thermal imaging technique that provided non-contact, non-invasive measurements with high spatial and thermal resolution. This technique was used to

 © 2022 The Authors. Advanced Electronic Materials published by Wiley-VCH GmbH

visualize the surface-temperature distribution of active devices by detecting the relative variations in the reflectivity of a sample in response to variations in the temperature.[33]

$$\Delta T = \frac{\Delta I_R}{I_{R0} \cdot C_{th}} \quad (1)$$

where ΔI_R and I_{R0} are the change and absolute value in the thermal reflectivity and C_{th} is thermoreflectance coefficient. For every material, C_{th} needs to be calibrated, separately.[33]

The thermoreflectance microscope NT100 from Microsanj LLC, USA, with transient resolution of 10 µs and temperature resolution of 1 K, was used in this study. The calibration was done using the electrochemically deposited Au, resulting in a C_{th} value of -2.8×10^{-4} K^{-1}. Since the reflectivity strongly depends on the surface roughness, all the values were taken from the top Au bridge. To characterize the dependence of electric current on the cooling, a pulsed current was passed and the change in temperature was averaged for at least 100 s. For the thermal transient measurements, a pulsed electric current was applied and the net cooling temperature was observed at different time delay. For the cycling reliability measurements, a pulsed electric current was applied, with a pulse time of 5 ms (1 ms on and 4 ms off) and an amplitude of the electric current which corresponds to the maximum net cooling temperature of the devices. The error of the temperature measurement using thermoreflectance technique was ≈4%.

2.4. Finite Element Simulation

FEM simulations were carried out with the commercially available COMSOL Multiphysics software package. In this manner it was possible to calculate approximations of the coupled heat and electric flux equations involved in thermoelectricity.

3. Results and Discussion

3.1. Device Optimization

The performance of a TED is determined primarily by ZT, which can be improved for a given material by optimizing the contact resistance and device geometry.[34] Whereas S_p and S_n are material properties that are independent of the geometry, R and K depend on the geometry of the device: their product should be minimum for a maximum value of ZT.

$R = \rho_p A_p^{-1} L_p + \rho_n A_n^{-1} L_n$, where L is the height, A is the cross-sectional area, and ρ is the electrical resistivity. $K = \kappa_p A_p L_p^{-1} + \kappa_n A_n L_n^{-1}$, where κ is the thermal conductivity, and the indices n and p correspond to n-type and p-type legs, respectively. To minimize the product RK, the following condition has to be met:

$$\frac{L_n \cdot A_p}{L_p \cdot A_n} = \sqrt{\frac{\kappa_n \cdot \rho_p}{\kappa_p \cdot \rho_n}} \quad (2)$$

Both legs of the TED should have the same length to ensure a good thermal contact between the thermoelectric elements and the heat source and sink. As a result, the cross-sectional area is the only geometric parameter that can be tuned for given materials properties.

In this work, we use n-type $Bi_2(Te_{.95}Se_{.05})_3$ and p-type Te as thermoelectric materials (see **Table 1** for their properties).

To understand how the device geometry influences its cooling performance and thereby changes ZT, we fabricated two µTECs with 160 leg pairs each and compared their performance. The details of the geometry of each µTEC are shown in Table 1. Whereas the $A_p A_n^{-1}$ ratio of µTEC_A was with 3.58 far from its optimal ratio of 1.37, the $A_p A_n^{-1}$ ratio of µTEC_B was found to be 2.64, which is close to its ideal ratio of 1.84. The deviation from the optimal ratio results from inaccuracies in the lithographic processing. In addition, the electrolyte used for the fabrication of µTEC_B was bubbled with N_2 before the electrochemical deposition.

The in-plane electrical conductivity of the materials was characterized using the van der Pauw method (Section I and Figures S1,S2, Supporting Information). Considering an anisotropic transport in BiTeSe of 2.3[37] between the in-plane and cross-plane direction we obtained an electrical conductivity of 700 S cm^{-1} and 1090 S cm^{-1} for the BiTeSe without N_2 bubbling and with N_2 bubbling, respectively. The electrical conductivity of 700 S cm^{-1} of the BiTeSe sample without N_2 bubbling, is in good agreement with the electrical conductivity reported by Schumacher et al[35] and is well within the error range of

Table 1. Materials properties and device design.

Materials	Section	Device	Dimension [width × length × height] [µm × µm × µm]	σ [S cm^{-1}]	S [µV K^{-1}]	κ [W m^{-1} K^{-1}]
BiTeSe	n-type	µTEC_A	33 × 33 × 7.5	700	−60	1.2[35]
		µTEC_B	33 × 33 × 9	1090	−50	1.4
Te	p-type	µTEC_A	33 × 118 × 7.5	250	210	1.8[36]
		µTEC_B	33 × 87 × 9	250		1.8[36]
Au	Bottom contact	µTEC_A	33 × 33/118 × 3	406 000	6.5[a)]	317[a)]
		µTEC_B	33 × 33/87 × 3			
Au	Top contact	µTEC_A	33 × 201 × 6	406 000	6.5[a)]	317[a)]
		µTEC_B	33 × 170 × 6			

[a)]Value from database of COMSOL multiphysics.

© 2022 The Authors. Advanced Electronic Materials published by Wiley-VCH GmbH

the electrical conductivity reported in other works for BiTeSe samples.[38] With the incorporation of N_2 bubbling an increase in the electrical conductivity was observed. To confirm the cross-plane electrical conductivity and the assumed anisotropic ratio, the BiTeSe sample with N_2 bubbling was additionally characterized using the Cox-Strack method (Section X, Supporting Information). With the Cox-Strack method, a cross-plane electrical conductivity of (1145 ± 246) S cm^{-1} was obtained, which is in good agreement with the electrical conductivity of 1090 S cm^{-1} obtained from the van der Pauw method. The thermal conductivity of the BiTeSe without N_2 bubbling was taken as 1.2 W m^{-1} K^{-1}.[35] Considering the Wiedemann Franz law the thermal conductivity of the BiTeSe with N_2 bubbling was slightly increased to 1.4 W m^{-1} K^{-1} (Section II, Supporting Information). The Seebeck coefficient was measured using a Potential Seebeck Microprobe system. For the BiTeSe without N_2 bubbling, the Seebeck coefficient was found to be −60 µV K^{-1}. While for the BiTeSe with N_2 bubbling a slight decrease in the Seebeck coefficient to −50 µV K^{-1} was observed.

The electrical transport properties of the electrochemically deposited material were improved by purifying the electrolytes prior to the electrochemical deposition. Oxygen, once incorporated into the TE material, is known to deteriorate the materials power factor $PF = S^2\ \sigma$.[39] Since the physically dissolved O_2 can be easily integrated into the electrochemically deposited material,[40] its replacement by N_2 helps to improve the electrical transport properties.[41] The electrolytes were hence bubbled with N_2 for 20 min so that the physically dissolved O_2 gas within the electrolytes would be replaced by N_2 gas. The EDX data of the electrochemically deposited BiTeSe showed reduction in the atomic percent of oxygen from 6.9 at% to 2.8 at% after N_2 bubbling (Section III, Figure S3, and Table S1, Supporting Information). The BiTeSe with N_2 bubbling showed a higher electrical conductivity and thermal conductivity in combination with a slightly decreased absolute Seebeck coefficient. Thus, the reduction in oxygen improved the electrical transport properties of the BiTeSe but resulted in a slightly decreased material zT from 0.063 to 0.058.

The obtained electrical conductivity and Seebeck coefficient of the electrochemically deposited Te were found to be 250 S cm^{-1} and 210 µV K^{-1}, respectively. The thermal conductivity was taken as 1.8 W m^{-1} K^{-1}.[36] The bubbled Te sample was also studied but no impact on the thermoelectric properties was observed.

Figure 2a) shows that the variation in the geometries of the µTECs led to a shift in the value of the electric current. The maximum cooling for µTEC_A and µTEC_B was seen at 180 and 235 mA, respectively. When the electric current was increased further, the cooling decreased because of the effect of joule heating in the device. As compared with µTEC_A, the maximum net cooling temperature of µTEC_B showed an increase from 6.4 to 10.8 K. The thermal image of both devices at maximum net cooling temperature can be found in the supporting information (Section IV and Figure S4, Supporting Information). The device ZT of µTEC_A and µTEC_B obtained by $ZT = 2\ \Delta T\ T^{-1}$ equals 0.044 and 0.074, respectively.

With the combined effect of geometric optimization and N_2 bubbling, an 69% improvement in the net cooling temperature

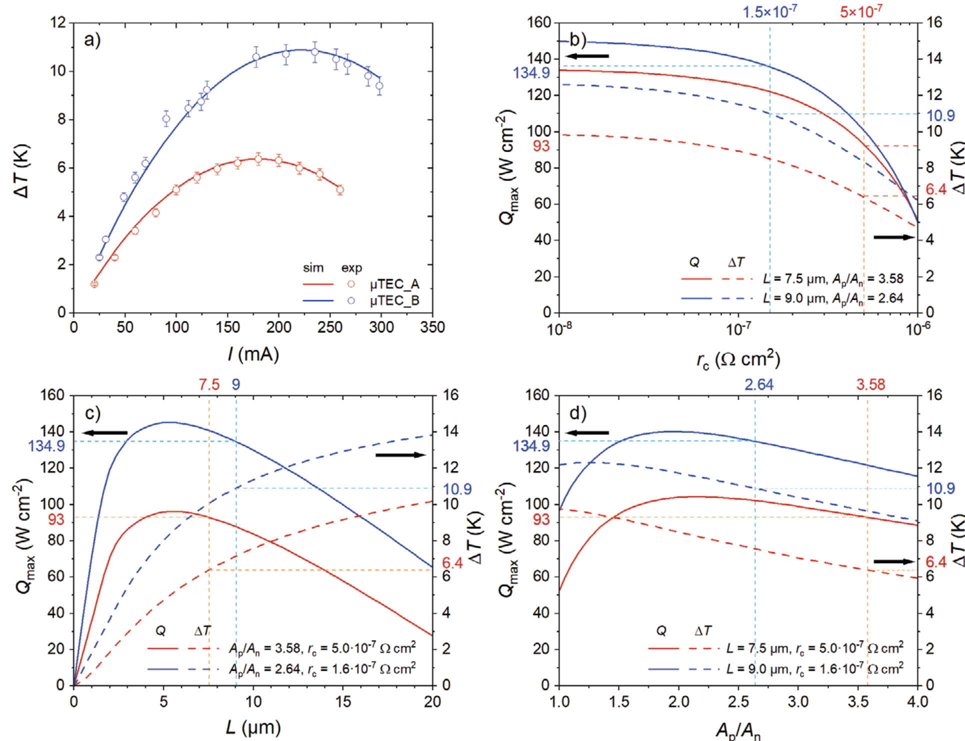

Figure 2. Cooling Performance study of freestanding devices. a) The net cooling temperature of µTEC_A and µTEC_B. Study of variation in the net cooling temperature and cooling power density of device with b) fixed height and A_p/A_n ratio by varying the r_c of the device c) fixed r_c and A_p/A_n ratio by varying the height of the device d) fixed r_c and height by varying the A_p/A_n ratio of the device.

 © 2022 The Authors. Advanced Electronic Materials published by Wiley-VCH GmbH

and 68% improvement in the device *ZT* was observed, although we observed a slight decrease in the materials *zT*. We mainly attribute this improvement to the device's reduced contact resistance (r_c) and optimized geometry. For the simulations shown in Figure 2a) the material properties from Table 1 were used. To match the simulation to the experimental results the r_c of the µTECs had to be adjusted to 5×10^{-7} Ω cm^2 for µTEC_A and 1.6×10^{-7} Ω cm^2 for µTEC_B. This is in good agreement with the experimentally found r_c of $(1.6 \pm 1.4) \cdot 10^{-7}$ Ω cm^2 of the N_2 bubbled sample, which was characterized with the Cox–Strack method (Section X, Supporting Information), and is well within recently published results of Corbett et al.[42] We attribute the reduction of the r_c to the purification of the electrolytes prior to the electrochemical deposition, that is, for the N_2 bubbled µTEC_B, the oxygen content was reduced, which might lead to the improved contact between the thermoelectric film and the top electrode. In addition to the increase in the net cooling temperature, a broader range of optimum current, which is directly related to the increased device figure of merit, was obtained making the device more suitable for applications.

In Figure 2b the net cooling temperature and the maximum cooling power density Q_{max} at optimal electrical current as function of r_c simulated for an $A_p\, A_n^{-1}$ ratio of 3.58 and a leg height of 7.5 µm corresponding to µTEC_A and an $A_p\, A_n^{-1}$ ratio of 2.64 and a leg height of 9 µm corresponding to µTEC_B is presented. Details of the simulation can be found in the supporting information (Section V and Figure S5, Supporting Information). With increasing r_c a decrease of Q_{max} and the net cooling temperature of the device was observed. The effective device figure of merit Z_e including r_c is given by $Z_e = Z(1 + r_c\, \rho^{-1}\, L^{-1})^{-1}$. Therefore, Z_e decreases as r_c increases, resulting in a decreased net cooling temperature and Q_{max}. The r_c of µTEC_A and µTEC_B are marked in Figure 2b) with blue and red dashed lines, respectively. Q_{max} was increased by 45% from 93 W cm^{-2} for µTEC_A to 134.9 W cm^{-2} for µTEC_B. Note that for the simulations in Figure 2 Q_{max} was defined as maximum power output per leg pair at optimal electrical current divided by the area of the top contact of one leg pair. Due to the decreased r_c from 5×10^{-7} Ω cm^2 to 1.6×10^{-7} Ω cm^2, the maximum net cooling temperature of µTEC_B was increased by 31% from 8.3 10.9 K and Q_{max} was increased from 100.6 W cm^{-2} to 134.9 W cm^{-2}. With the same r_c as µTEC_B, the net cooling temperature of µTEC_A would be increased by 33% to 8.5 K and Q_{max} would increase to 122.3 W cm^{-2}.

In Figure 2c the simulated net cooling temperature and the Q_{max} in dependency of the height of the thermoelectric legs with a constant $A_p\, A_n^{-1}$ ratio of 3.6 and r_c of 5×10^{-7} Ω cm^2 corresponding to µTEC_A and a constant $A_p\, A_n^{-1}$ ratio of 2.6 and r_c of 1.6×10^{-7} Ω cm^2 corresponding to µTEC_B are shown. As the height of the thermoelectric legs increased, the thermal conductivity of the device decreased, which leads to an increased net cooling temperature. While Q_{max} initially increased until it reached a maximum at a thermoelectric leg height of ≈5 µm for both µTECs. With further increased leg heights Q_{max} started decreasing again. The trend results from the increased electrical resistance with increasing leg height, which leads to a reduced optimal current. As a result, Joule heating reached a maximum at an intermediate height. Q_{max} is determined by the balance of Joule heating, Peltier cooling, which decreases with the current, and the thermal conductance, which follows a $1/L$ dependency. Therefore, choosing the optimal thickness of the thermoelectric legs is a trade-off between maximum net cooling temperature and Q_{max}. The heights of 7.5 and 9 µm of µTEC_A and µTEC_B are marked in Figure 2c) with blue and red dashed lines, respectively. By increasing the leg height of µTEC_B from 7.5 to 9 µm, the maximum net cooling temperature was increased by 9% from 10 to 10.9 K but in the same time Q_{max} decreased by 6%. With the same leg height as µTEC_B, the net cooling temperature of µTEC_A would be increased by 19% to 7.6 K with a slightly reduced Q_{max} of 87.8 W cm^{-2}.

Figure 2d) shows the simulated net cooling temperature and Q_{max} depending on the $A_p\, A_n^{-1}$ ratio with a constant height of 7.5 µm and r_c of 5×10^{-7} Ω cm^2 corresponding to µTEC_A and a constant height of 9 µm and r_c of 1.6×10^{-7} Ω cm^2 corresponding to µTEC_B. When the $A_p\, A_n^{-1}$ ratio is increased, the net cooling temperature first increased until it reaches a maximum when the thermal and electrical resistance are balanced, and then decreases again. Since the simulation also includes the contribution from the contact resistance and the resistance of the contacts, this result deviates from the analytical obtained result from Equation (1). The additional resistance shifts the optimal $A_p\, A_n^{-1}$ ratio for µTEC_A from 1.37 to 1 and for µTEC_B from 1.84 to 1.2. The Q_{max} also increased until it reached a maximum, but at a higher $A_p\, A_n^{-1}$ ratio of 2.1 for µTEC_A and 1.9 for µTEC_B. With further increased $A_p\, A_n^{-1}$ ratio Q_{max} started decreasing again. The reduced electrical resistance with increasing $A_p\, A_n^{-1}$ ratio lead to an increased optimal current and thus to an increased Peltier cooling, while the thermal conductance showed a linear increase. The slope of Q_{max} is a result of the almost logarithmically increasing cooling power, which was obtained by balancing the Joule heating, Peltier cooling, and thermal conduction, divided by the linearly increased top contact area. Therefore, choosing the optimal $A_p\, A_n^{-1}$ ratio is again a trade-off between maximum net cooling temperature and Q_{max}. The $A_p\, A_n^{-1}$ ratios 3.58 of µTEC_A and 2.64 of µTEC_B are marked in Figure 2d) with blue and red dashed lines, respectively. By decreasing the $A_p\, A_n^{-1}$ ratio of µTEC_B from 3.58 to 2.64, the maximum net cooling temperature was increased by 17% from 9.3 to 10.9 K and Q_{max} increased from 121.4 W cm^{-2} to 134.9 W cm^{-2}. With the same $A_p\, A_n^{-1}$ ratio as µTEC_B, the net cooling temperature of µTEC_A would be increased by 19% to 7.6 K combined with an increased Q_{max} of 102 W cm^{-2}.

3.2. Embedding the Devices within a Filling Material

Devices for use in commercial applications require a suitable packaging so that the devices sustain the direct thermal contact with the target heat sink and source. The as fabricated devices are free-standing, limiting their usage. Hence, we embedded the free-standing devices so that they build a flat surface at the top level. The embedding provides mechanical as well as chemical stability to the devices. With a filling material having a value of the thermal conductivity, $\kappa_{filling}$, the heat flux through the filling material provides a thermal shortcut. Consequently, the lower $\kappa_{filling}$, the better. We used a Finite Element Method (FEM) to select the filling material

 © 2022 The Authors. Advanced Electronic Materials published by Wiley-VCH GmbH

and evaluated the quantitative effect of the material on the net cooling temperature of the µTEC. Whereas the device geometry and the electrical input current were kept constant, $\kappa_{filling}$ was varied over five orders of magnitude, from 0.001 W m^{-1} K^{-1} to 100 W m^{-1} K^{-1}, keeping I at 180 mA. The simulation revealed that the maximum net cooling temperature decreased rapidly as $\kappa_{filling}$ was increased (Section VI and Figure S6, Supporting Information). An increase in $\kappa_{filling}$ from 0 to 1 W m^{-1} K^{-1} led to a cooling of 2 K, from which point onward a further increase in the $\kappa_{filling}$ led to a drastic reduction in the net cooling temperature. When $\kappa_{filling}$ reached 10 W m^{-1} K^{-1}, the corresponding cooling was 1.19 K. Almost no cooling was observed for a filling material with $\kappa_{filling}$ = 100 W m^{-1} K^{-1}.

Based on the simulations, embedding with a polymer proved to be most effective because of its sufficiently low $\kappa_{filling}$, that is, instead of being free standing, the whole device was encapsulated leaving just the top Au open. We used photoresist (AZ9260), which has good processability and could be spin-coated with a thickness in the range of the device. Its viscosity enabled complete embedment of the device. Then we structured the photoresist to open the top Au portions and flood exposed the remaining parts such that the photoresist ended up on the same height as the device building a smooth surface at the top level, which is important for many applications. Importantly, the baking parameters of the photoresist did not affect the device properties negatively. The $\kappa_{filling}$ of the photoresist at room temperature was 0.15 W m^{-1} K^{-1},[43] which was used in the simulation of embedded µTECs (eµTECs). The fabricated µTECs were used to study the effect of embedding with a filling material. The cooling characteristics with respect to the electric current were studied for embedded µTEC_A (eµTEC_A) and µTEC_B (eµTEC_B). The maximum cooling was obtained at the same value of electric current but the maximum cooling temperature of eµTEC_A and eµTEC_B was lower (**Figure 3a**). Adding the filling material reduced the overall cooling from 6.4 to 5.5 K for µTEC_A and from 10.8 to 9.6 K for µTEC_B. Notably, the shape of the cooling curve remained the same.

This reduction in cooling is evident from the simulation results (Figure S6a,b, Supporting Information) and the thermal image (Figure S6c, Supporting Information). The cooling curve of the embedded µTECs was simulated by using the material properties from Table 1 and a contact resistance of 5 × 10^{-7} Ω cm^2 for eµTEC_A and of 1.6 × 10^{-7} Ω cm^2 for eµTEC_B. Good agreement between the simulation and experimental data was obtained for eµTEC_A and eµTEC_B when κ of the filling material was 0.15 W m^{-1} K^{-1}. Thermal data reveal no signal around µTEC_A but some heat dissipation from eµTEC_A to the filling material (Figure S6c, Supporting Information). This explains the slight degradation of the cooling performance of embedded devices.

Embedding devices in the packaging material increases their thermal mass, which might lead to a reduced response time. To analyze the transient thermal response of the device a pulsed electric current was applied and the net cooling temperature was measured at different time delays using thermoreflectance microscopy (Figure 3b). The time dependent increase of the net cooling temperature was fitted (Figure 3b solid and dashed lines) by $\Delta T = \Delta T_{max}$ (1 – exp(t τ^{-1})), where ΔT_{max} is the steady-state maximum net cooling temperature, and τ the thermal response time of the device. In the following we defined 4 τ as thermal response time to reach the steady-state cooling temperature (98.2% of ΔT_{max}). The steady-state cooling temperature was reached at 734 µs for µTEC_A and 639 µs for µTEC_B, without filling material. The lower thermal response time of µTEC_B is due to the reduced cross-section of the device. For the polymer-embedded devices, the thermal response time to reach steady-state has been increased by 35% to 992 µs for eµTEC_A and by 13% to 721 µs for eµTEC_B due to the additional thermal mass of the filling material.

3.3. Performance of the Embedded Devices

The efficiency of a TEC is typically described by the coefficient of performance (COP) given by the ratio of the absorbed heat at the cold side to the electrical input power. In order to analyze the efficiency of our µTECs and the effect of embedding, we simulated the COP of the devices. Details of the simulation can be found in the supporting information (Sections VII,VIII and Figures S7–S9, Supporting Information). **Figure 4a** shows the COP of µTEC_A and µTEC_B compared to the embedded µTECs eµTEC_A and eµTEC_B, simulated for a constant

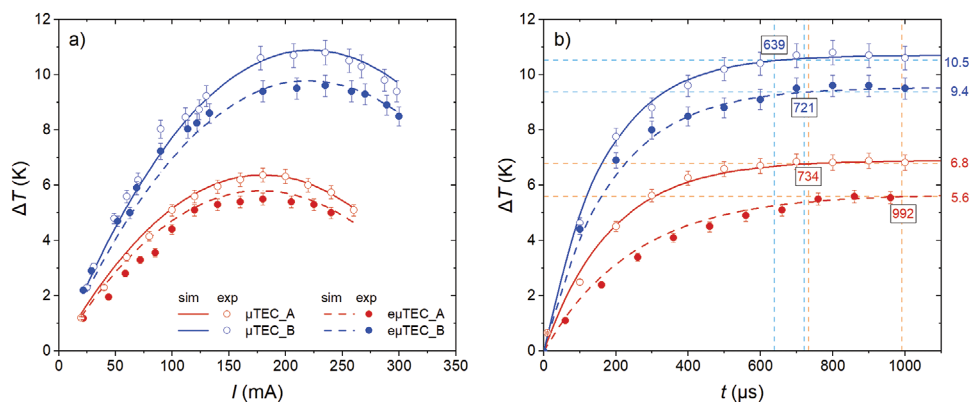

Figure 3. Cooling performance of free-standing and embedded µTECs. a) Shows the simulation results (lines) and the experimental (dots) cooling response of eµTEC_A eµTEC_B in comparison to µTEC_A, µTEC_B_4; b) The comparison of the transient response time of free-standing and embedded µTECs at different time delays.

© 2022 The Authors. Advanced Electronic Materials published by Wiley-VCH GmbH

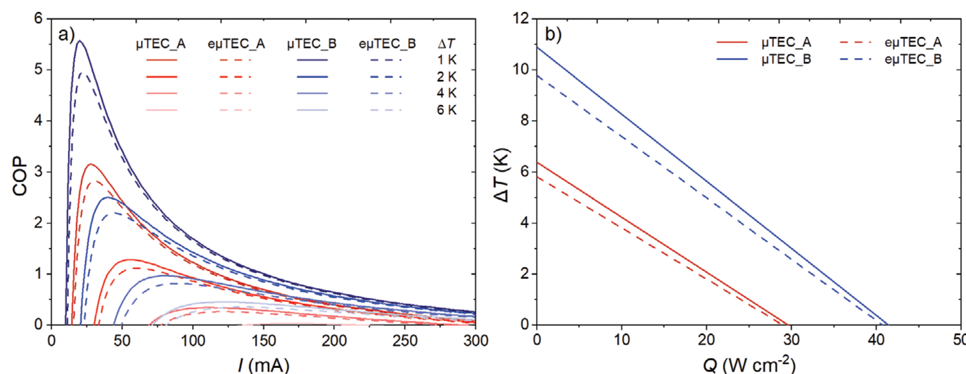

Figure 4. Realizing high Coefficient of Performance and Cooling power density of as fabricated devices. a) The effect of current on COP of freestanding and embedded devices (µTEC_A, eµTEC_A, µTEC_B, and eµTEC_B). b) Comparison of cooling power density and net cooling temperature of free-standing and embedded devices (µTEC_A, eµTEC_A, µTEC_B, and eµTEC).

temperature difference of 1, 2, 4, and 6 K in dependency of the applied current. To maintain a constant temperature difference, the absorbed heat at the cold side was adjusted depending on the applied current (Figure S8, Supporting Information). The maximum COP of 3.2 for µTEC_A and 5.6 for µTEC_B was found at the lowest temperature difference of 1 K. The maximum COP of the embedded devices decreased for eµTEC_A and eµTEC_B to 2.8 and 4.9, respectively, due to the additional heat losses caused by the filling material. In addition, as the temperature difference increased, the heat absorbed on the cold side decreased, resulting in a reduced COP, and the current at which the maximum COP was observed increased linearly.

Figure 4b shows the dependence of the net cooling temperature on the simulated cooling power density Q for the free-standing and embedded µTECs. Note that the Q shown in Figure 4b is the cooling power density of the device, that is, the distance of 50 µm between the adjacent leg pairs was considered, which gives a filling factor of 23.9% of µTEC_A and 21.7% for µTEC_B.

The maximum net cooling temperature of µTEC_A was 6.4 K and of µTEC_B 10.8 K. The maximum Q at zero temperature difference was 29.6 Wcm^{-2} for µTEC_A and 41.4 Wcm^{-2} for µTEC_B. Due to the additional heat losses when embedding the devices, the maximum net cooling temperature of µTEC_A and µTEC_B was reduced to 5.5 and 9.6 K, respectively. The maximum Q also showed slight decrease to 29 W cm^{-2} for µTEC_A and 40.75 W cm^{-2} for µTEC_B. By further reducing the distance between the leg pairs the maximum Q could be increased, that is, if the distance between the leg pair is 20 µm (Section IX and Figure S10, Supporting Information) the maximum Q would increase to 89.2 W cm^{-2}, which is more than double the cooling power density of µTEC_B.

3.4. Reliability of the Embedded Devices

Previous studies have demonstrated the exceptional reliability of the free-standing µTECs.[1] The µTEC survived for 1 month in a cooling stability experiment under the continuous application of a direct current. In the cycling reliability test, the device started to deteriorate after 10 million cycles. Since practical applications require that the devices be embedded, we explored how this embedding affects the reliability of different µTECs (**Figure 5**).

To characterize the cycling reliability, we applied a pulsed electrical current (1 ms on and 4 ms off) to µTEC_A for 120 million cycles. The net cooling temperature, which was measured by thermoreflectance microscopy, was seen to remain intact even after 120 million cycles. µTEC_B also showed a high cycling reliability of over 70 million cycles.

Optimizing the geometry of the µTEC led to an exceptionally high cycling reliability. In the previous work, the deterioration in reliability was most likely because of a loose contact between the thermoelectric leg and the top metallization. In this study, we increased the contact area between these parts and achieved a higher cycling reliability for the µTECs. The cycling reliability was also tested for the polymer-embedded µTECs. eµTEC_A was found to survive 85 million cycles, whereas eµTEC_B survived 70 million cycles, following which all two devices showed a drop in the net cooling temperature. It is apparent that the polymer-embedded µTEC was less tolerant to the internal strain caused by the materials' thermal expansion coefficients than

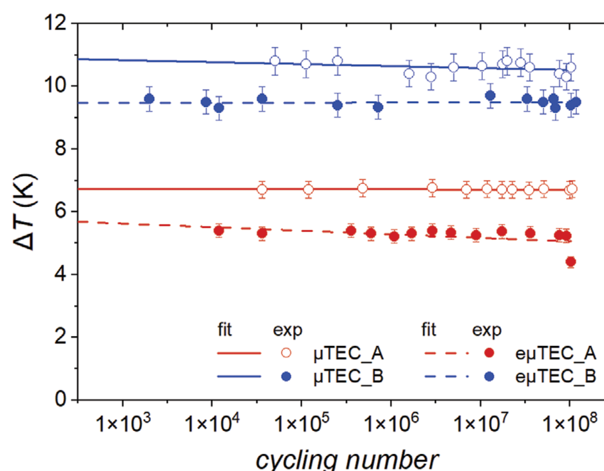

Figure 5. Comparison of cycling reliability of the free-standing and embedded µTECs. One cycle corresponds to an electric pulsed current with an on time of 1 ms and off time of 4 ms.

© 2022 The Authors. Advanced Electronic Materials published by Wiley-VCH GmbH

the free-standing μTEC. This is because the free-standing μTEC had more freedom to adapt to this internal strain, whereas the polymer-embedded eμTEC had less breathing space to cope with the internal strain. Nevertheless, before it started to deteriorate the cycling performance of the embedded eμTEC was exceptionally high. Such performance is more than sufficient for most applications.

4. Conclusion

We combined photolithographic patterning and electrochemical deposition to fabricate free-standing μTECs and then compared the net cooling temperature of two μTECs with different geometries. We found that that the best performing device had a reduced ratio between n-type and p-type cross-sections of the thermoelectric legs closer to the optimal ratio, increased leg height, and decreased contact resistance. At room temperature, this μTEC yielded a net cooling temperature of 10.8 K at 235 mA. The device showed a rapid cooling-response time of 639 μs and a cycling reliability of 120 million cycles. The effect of geometry and contact resistance on the cooling power density and the net cooling temperature was studied, giving a guideline for the fabrication of TECs with optimal cooling power density and net cooling temperature. Real-world applications require that the μTECs be packaged so that they can be brought in direct thermal contact with the heat sink. We thus embedded the μTECs with the polymer AZ9260 photoresist and characterized the performance of the μTECs before and after embedding. The net cooling temperature after embedding within the polymer was 9.6 K at 235 mA, a drop that could be attributed to thermal loss through the polymer. However, the embedded devices showed a rapid cooling response time of 721 μs and a slightly reduced cycling reliability of 85 million cycles. These embedded, optimized, stable and easily scalable μTEDs open new avenues for wide-spread applications in biomedical applications, powering internet-of-things devices, and local heat management.

Supporting Information

Supporting Information is available from the Wiley Online Library or from the author.

Acknowledgements

The authors thank H. Stein, S. Wohlrab, D. Hofmann, C. Kupka, and R. Uhlemann in IFW Dresden for helpful technical support, further help from L Schnatmann is gratefully acknowledged. G.S. acknowledges funding from the DFG (Deutsche Forschungsgemeinschaft) within grant number SCHI1010/11-1 and H.R. within grant number RE3973/1-1. J.G. acknowledges the financial support from the Principality of Asturias and European Union under the PCTI/FEDER program "Retorno Talento" (project no. IDI/2018/000010). G.L. thanks the funding support of the National Natural Science Foundation of China (Grant No. 52172259). D.A.L.R acknowledges the funding of the Mexican National Council for Science and Technology (Consejo Nacional de Ciencia y Tecnologia—CONACYT) for the research grant CVU61110.

Open access funding enabled and organized by Projekt DEAL.

Conflict of Interest

The authors declare no conflict of interest.

Data Availability Statement

The data that support the findings of this study are available from the corresponding author upon reasonable request.

Keywords

contact resistance, electrochemical deposition, micro-thermoelectric devices, packaging, TEC design, TEC reliability, thermoelectrics

Received: September 24, 2021
Revised: January 6, 2022
Published online: February 12, 2022

[1] G. Li, J. G. Fernandez, D. A. L. Ramos, V. Barati, N. Pérez, I. Soldatov, H. Reith, G. Schierning, K. Nielsch, *Nat. Electron.* **2018**, *1*, 555.
[2] G. J. Snyder, J. R. Lim, C.-K. Huang, J.-P. Fleurial, *Nat. Mater.* **2003**, *2*, 528.
[3] G. J. Snyder, E. S. Toberer, in *Materials for Sustainable Energy: A Collection of Peer-Reviewed Research and Review Articles from Nature Publishing Group*, World Scientific, Singapore **2011**, p. 101.
[4] F. J. DiSalvo, *Science* **1999**, *285*, 703.
[5] N. Su, S. Guo, F. Li, D. Liu, B. Li, J. Li, M. Ji, *J. Micromech. Microeng.* **2018**, *28*, 125002.
[6] R. Enright, S. Lei, I. Mathews, G. Cunningham, R. Frizzell, A. Shen, *ECS Trans.* **2015**, *69*, 37.
[7] J. Garcia, D. A. L. Ramos, M. Mohn, H. Schlörb, N. P. Rodriguez, L. Akinsinde, K. Nielsch, G. Schierning, H. Reith, *ECS J. Solid State Sci. Technol.* **2017**, *6*, N3022.
[8] J. P. Rojas, D. Singh, S. B. Inayat, G. A. T. Sevilla, H. M. Fahad, M. M. Hussain, *ECS J. Solid State Sci. Technol.* **2017**, *6*, N3036.
[9] V. Leonov, R. J. Vullers, *J. Renewable Sustainable Energy* **2009**, *1*, 062701.
[10] S. J. Kim, J. H. We, B. J. Cho, *Energy Environ. Sci.* **2014**, *7*, 1959.
[11] Y. Khan, A. E. Ostfeld, C. M. Lochner, A. Pierre, A. C. Arias, *Adv. Mater.* **2016**, *28*, 4373.
[12] N. Mejia, K. Dedow, L. Nguy, P. Sullivan, S. Khoshnevis, K. R. Diller, *J. Med. Devices* **2015**, *9*, 044502.
[13] E. S. Hwang, S. Kwon, D. Kim, Y. T. Cho, Y. G. Jung, *J. Mech. Sci. Technol.* **2015**, *29*, 1697.
[14] A. Cadei, A. Dionisi, E. Sardini, M. Serpelloni, *Meas. Sci. Technol.* **2013**, *25*, 012003.
[15] M. Amasia, M. Cozzens, M. J. Madou, *Sens. Actuators, B* **2012**, *161*, 1191.
[16] J. H. Seo, *J. Mech. Sci. Technol.* **2015**, *29*, 571.
[17] E. Koukharenko, X. Li, J. Kuleshova, M. Fowler, N. Frety, J. M. Tudor, S. P. Beeby, I. Nandhakumar, N. M. White, *MRS Online Proc. Libr.* **2010**, *1267*, 1018.
[18] M.-Y. Kim, T.-S. Oh, *J. Electron. Mater.* **2013**, *42*, 2752.
[19] H. Bottner, J. Nurnus, A. Gavrikov, G. Kuhner, M. Jagle, C. Kunzel, D. Eberhard, G. Plescher, A. Schubert, K.-H. Schlereth, *J. Microelectromech. Syst.* **2004**, *13*, 414.
[20] K. Uda, Y. Seki, M. Saito, Y. Sonobe, Y.-C. Hsieh, H. Takahashi, I. Terasaki, T. Homma, *Electrochim. Acta* **2015**, *153*, 515.
[21] G. Zeng, J. E. Bowers, J. M. Zide, A. C. Gossard, W. Kim, S. Singer, A. Majumdar, R. Singh, Z. Bian, Y. Zhang, A. Shakouri, *Appl. Phys. Lett.* **2006**, *88*, 113502.

© 2022 The Authors. Advanced Electronic Materials published by Wiley-VCH GmbH

[22] I.-Y. Huang, M.-J. Li, K.-M. Chen, G.-Y. Zeng, K.-D. She, *2nd IEEE Int. Conf. on Nano/Micro Engineered and Molecular Systems*, IEEE, Piscataway, NJ **2007**, pp. 749-752.
[23] I. Y. Huang, J. C. Lin, K. D. She, M. C. Li, J. H. Chen, J. S. Kuo, *Sens. Actuators, A* **2008**, *148*, 176.
[24] R. Roth, R. Rostek, G. Lenk, M. Kratschmer, K. Cobry, P. Woias, *Transducers & Eurosensors XXVII: The 17th Int. Conf. on Solid-State Sensors, Actuators and Microsystems*, IEEE, Piscataway, NJ **2013**, pp. 486-489.
[25] H. Bottner, J. Nurnus, A. Gavrikov, G. Kuhner, M. Jagle, C. Kunzel, D. Eberhard, G. Plescher, A. Schubert, K.-H. Schlereth, *J. Microelectromech. Syst.* **2004**, *13*, 414.
[26] S. Corbett, D. Gautam, S. Lal, K. Yu, N. Balla, G. Cunningham, K. M. Razeeb, R. Enright, D. McCloskey, *ACS Appl. Mater. Interfaces* **2021**, *13*, 1773.
[27] X.-L. Shi, J. Zou, Z.-G. Chen, *Chem. Rev.* **2020**, *120*, 7399.
[28] V. Barati, J. G. Fernandez, K. Geishendorf, L. U. Schnatmann, M. Lammel, A. Kunzmann, N. Pérez, G. Li, G. Schierning, K. Nielsch, H. Reith, *Adv. Electron. Mater.* **2020**, *6*, 1901288.
[29] O. Yamashita, S. Tomiyoshi, K. Makita, *J. Appl. Phys.* **2003**, *93*, 368.
[30] L.-D. Zhao, S.-H. Lo, Y. Zhang, H. Sun, G. Tan, C. Uher, C. Wolverton, V. P. Dravid, M. G. Kanatzidis, *Nature* **2014**, *508*, 373.
[31] R. He, G. Schierning, K. Nielsch, *Adv. Mater. Technol.* **2018**, *3*, 1700256.
[32] G. S. Nolas, J. Sharp, J. Goldsmid, *Thermoelectrics: Basic Principles and New Materials Developments*, Vol. *45*, Springer, Berlin **2013**.
[33] M. Farzaneh, K. Maize, D. Lüerßen, J. Summers, P. Mayer, P. Raad, K. Pipe, A. Shakouri, R. Ram, J. A. Hudgings, *J. Phys. D: Appl. Phys.* **2009**, *42*, 143001.
[34] D. A. Lara Ramos, V. Barati, J. Garcia, H. Reith, G. Li, N. Pérez, G. Schierning, K. Nielsch, *Adv. Sustainable Syst.* **2019**, *3*, 1800093.
[35] C. Schumacher, K. G. Reinsberg, R. Rostek, L. Akinsinde, S. Baessler, S. Zastrow, G. Rampelberg, P. Woias, C. Detavernier, J. A. Broekaert, *Adv. Energy Mater.* **2013**, *3*, 95.
[36] S. Lin, W. Li, Z. Chen, J. Shen, B. Ge, Y. Pei, *Nat. Commun.* **2016**, *7*, 10287.
[37] X. Yan, B. Poudel, Y. Ma, W. S Liu, G. Joshi, H. Wang, Y Lan, D Wang, G Chen, Z. F Ren, *Nano Lett.* **2010**, *10*, 3373.
[38] W. H. Chao, Y. R. Chen, S. C. Tseng, P. H. Yang, R. J. Wu, J. Y. Hwang, *Thin Solid Films* **2014**, *570*, 172.
[39] M. Zhang, D. Wang, C. Chang, T. Lin, K. Wang, L.-D. Zhao, *J. Mater. Chem. C* **2019**, *7*, 10507.
[40] T. Koga, C. Hirakawa, Y. Sakata, H. Noma, K. Nonaka, N. Terasaki, *ECS Trans.* **2017**, *75*, 15.
[41] M. A. Alpuche-Aviles, F. Farina, G. Ercolano, P. Subedi, S. Cavaliere, D. J. Jones, J. Rozière, *Nanomaterials* **2018**, *8*, 668.
[42] S. Corbett, D. Gautam, L. Swatchith, Y. Kenny, N. Balla, G. Cunningham, K. M. Razeeb, R. Enright, D. McCloskey, *ACS Appl. Mater. Interfaces* **2021**, *13*, 1773.
[43] S. L Chung, J. S Lin, *Molecules* **2016**, *21*, 670.

© 2022 The Authors. Advanced Electronic Materials published by Wiley-VCH GmbH